

**Bifunctional Catalysis**

 International Edition: DOI: 10.1002/anie.201915080  
 German Edition: DOI: 10.1002/ange.201915080

# Impact of the Spatial Organization of Bifunctional Metal–Zeolite Catalysts on the Hydroisomerization of Light Alkanes

Kang Cheng, Lars I. van der Wal, Hideto Yoshida, Jogchum Oenema, Justine Harmel, Zhaorong Zhang, Glenn Sunley, Jovana Zečević, and Krijn P. de Jong\*

**Abstract:** Improving product selectivity by controlling the spatial organization of functional sites at the nanoscale is a critical challenge in bifunctional catalysis. We present a series of composite bifunctional catalysts consisting of one-dimensional zeolites (ZSM-22 and mordenite) and a  $\gamma$ -alumina binder, with platinum particles controllably deposited either on the alumina binder or inside the zeolite crystals. The hydroisomerization of *n*-heptane demonstrates that the catalysts with platinum particles on the binder, which separates platinum and acid sites at the nanoscale, leads to a higher yield of desired isomers than catalysts with platinum particles inside the zeolite crystals. Platinum particles within the zeolite crystals impose pronounced diffusion limitations on reaction intermediates, which leads to secondary cracking reactions, especially for catalysts with narrow micropores or large zeolite crystals. These findings extend the understanding of the “intimacy criterion” for the rational design of bifunctional catalysts for the conversion of low-molecular-weight reactants.

## Introduction

Bifunctional catalysis is involved in a wide range of important catalytic processes, such as biomass upgrading, hydrogenation of CO/CO<sub>2</sub> to hydrocarbons, and hydroisomerization of *n*-paraffins to high-quality fuels.<sup>[1]</sup> In many cases, bifunctional coupling of two different reactions can provide enhanced catalytic activities and unexpected product selectivities.<sup>[2]</sup> One of most applied bifunctional catalysts consists of a transition metal, for example, platinum, palladium, or

molybdenum (sulfide), supported on solid acids such as alumina, alumina-silica, or zeolites.<sup>[3]</sup> Therefore, bifunctional catalysis naturally brings out the issue of how to rationally organize the two components to maximize synergy without disturbing the communication between the two types of active sites and the diffusion of molecules involved in the reaction.<sup>[4]</sup>

Representative catalysts for hydroisomerization are composed of platinum and acidic zeolites. The metal sites catalyze the dehydrogenation of alkanes to alkenes and subsequent hydrogenation of *iso*-alkenes to desired *iso*-alkanes, while the Brønsted acid sites (BAS) in the zeolites catalyze skeletal rearrangements or cracking reactions via carbenium ions as intermediates.<sup>[5]</sup> The catalytic performance of bifunctional catalysts is determined by many parameters such as zeolite topology, acid strength and density, metal properties, and the ratio of metal sites to acid sites.<sup>[3b,6]</sup> Furthermore, the distance between the two functional sites, often described as proximity or intimacy degree, also plays an important role in catalysis.<sup>[6c,7]</sup> To date, research has particularly focused on the aforementioned parameters, while for decades, the intimacy criterion by Weisz was often applied as “the closer the better” for optimizing the spatial arrangement of metal and acid sites.<sup>[8]</sup> However, one should note that the intimacy criterion for bifunctional catalysts, which was verified at the micron scale, mainly correlates with the catalytic activity. The impact of intimacy between metal and acid sites at the nanoscale and on product selectivities is still not described well.


Regarding intimacy at the nanoscale, Höchtl et al. reported that the distance between acid and metal sites has only a minor influence for the hydroisomerization of *n*-heptane as long as metal and zeolite are in direct contact.<sup>[9]</sup> In contrast, our group recently studied the hydroconversion of C<sub>10</sub>–C<sub>19</sub> paraffins over bifunctional catalysts containing zeolite Y and an alumina binder, with platinum metal controllably deposited either within the zeolite crystals or on the binder.<sup>[10]</sup> It was found that the platinum-on-binder catalyst offered higher isomerization selectivity and lower cracking selectivity than the platinum-in-zeolite catalyst. Subsequently, Samad, Mousa, and colleagues reported that an atomic-scale proximity between metal and acid sites was not required to reach a good bifunctionality in isomerization reactions, while catalysts with the two functional sites at a nanoscale distance performed better.<sup>[11]</sup> Nevertheless, up to now, few studies have touched upon the impact of nanoscale proximity between functional sites due to limited synthesis protocols and challenges in characterization. In particular, the impact of the location of platinum on intracrystalline diffusion of linear and branched

\*] Dr. K. Cheng, L. I. van der Wal, J. Oenema, Dr. J. Harmel, Dr. J. Zečević, Prof. K. P. de Jong  
 Inorganic Chemistry and Catalysis  
 Debye Institute for Nanomaterials Science, Utrecht University  
 3584 CG, Utrecht (The Netherlands)  
 E-mail: k.p.dejong@uu.nl

Dr. H. Yoshida  
 The Institute of Scientific and Industrial Research, Osaka University  
 8-1 Mihogaoka, Ibaraki, Osaka 567-0047 (Japan)

Dr. Z. Zhang  
 Applied Chemistry and Physics Centre of Expertise  
 BP Group Research  
 150 West Waukegan Road, Naperville, IL 60563 (USA)

Dr. G. Sunley  
 Hull Research and Technology Center, BP plc, c/o BP Chemicals  
 Saltend, Hull HU 12 8DS (UK)

 Supporting information and the ORCID identification number(s) for the author(s) of this article can be found under:  
<https://doi.org/10.1002/anie.201915080>

alkanes with low molecular weight has not been demonstrated.

In this work, we focus on the effect of nanoscale intimacy on the hydroisomerization of light alkanes over industrially relevant bifunctional catalysts consisting of one-dimensional (1D) zeolites, a  $\gamma$ -alumina binder, and platinum particles. ZSM-22 (TON-type) and mordenite (MOR-type), which have different micropore openings, are employed as acidic components due to their wide applications in industry.<sup>[12]</sup> Aside from industrial applications, these 1D zeolites have been studied for their intriguing characteristics for the diffusion of molecules, sometimes referred to as single-file diffusion.<sup>[13]</sup> We selectively place platinum particles either on the alumina binder or within the zeolite crystals, providing distinct intimacy levels of metal and acid sites at the nanoscale. Moreover, two mordenite zeolites with different crystal sizes are used to investigate the effect of diffusion length on the catalytic performance. To unequivocally determine the platinum location and sizes, we use high-angle annular dark-field scanning transmission electron microscopy (HAADF-STEM) to image the 70-nm-thick ultramicrotomed sections of these composite catalysts. Bifunctional catalysts are evaluated under industrially relevant conditions for the hydroisomerization of *n*-heptane. Interestingly, keeping platinum out of the zeolite crystals is beneficial for the selectivity of C<sub>7</sub> isomers, while embedding platinum inside the zeolite crystals favors cracking reactions.

## Results and Discussion

### H-ZSM-22-Based Catalysts with 10-MR Micropores

SEM imaging depicts the typical agglomerates of rod-like H-ZSM-22 crystals with an average crystal length of 1.6  $\mu\text{m}$  (Figure 1 a). The micropore channels with 10-membered-ring (10-MR) openings normally run parallel to the long axis of the crystal, and there is no communication between these channels (Figure 1 b). By using an ion-exchange method with  $\text{Pt}(\text{NH}_3)_4(\text{NO}_3)_2$  and the parent zeolite H-ZSM-22,  $\text{Pt}(\text{NH}_3)_4^{2+}$  ions can be introduced by interacting with cation-exchange sites. It is notable that the kinetic diameter of the  $\text{Pt}(\text{NH}_3)_4^{2+}$  ion (0.48 nm) is close to the size of the H-ZSM-22 pores ( $0.45 \times 0.55 \text{ nm}$ ),<sup>[14]</sup> so the diffusion of  $\text{Pt}(\text{NH}_3)_4^{2+}$  ions into H-ZSM-22 micropore channels might be impeded. Figure 1 c shows that the parallel micropore channels are oriented along the long axis of crystals (*c*-axis), and Pt particles are well dispersed on or in the H-ZSM-22 crystals with average size of 1.6 nm. However, the spatial distribution of the Pt particles along the H-ZSM-22 crystals cannot be clarified from only one orientation. Up to now, there is no study on the spatial distribution of Pt particles within individual H-ZSM-22 crystals.

To clarify this distribution, HAADF-STEM was used to investigate the 70-nm-thick ultramicrotomed sections of the reduced Pt-H-ZSM-22 catalyst. Cutting the resin-embedded catalysts with an ultramicrotome, which produces thin slices, exposes the cross-sections of the catalyst granules and provides information on the spatial arrangement of functional

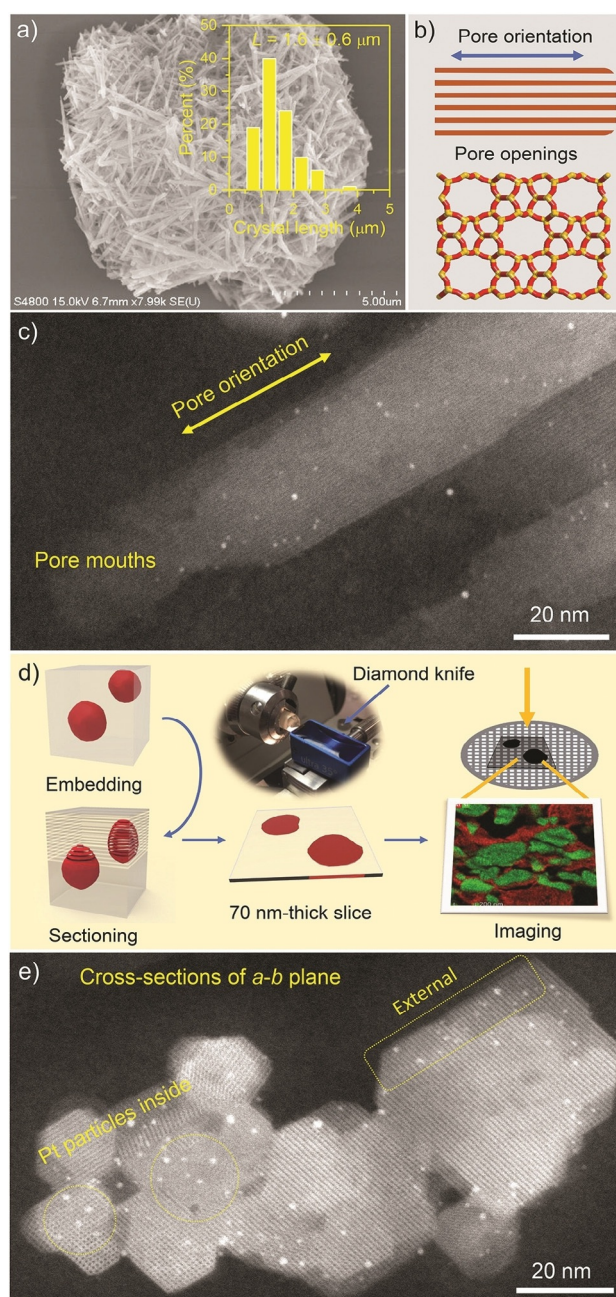


**Figure 1.** Structure of H-ZSM-22 and spatial distribution of Pt particles in the H-ZSM-22 crystals. a) SEM image of H-ZSM-22 crystals. b) Pore orientation (*c*-axis) and pore openings of H-ZSM-22. c) HAADF-STEM image of Pt-H-ZSM-22 along the *c*-axis without ultramicrotomy. d) Schematic diagram of the sectioning of resin-embedded catalyst particles using a diamond knife. e) HAADF-STEM image of the *ab*-plane of ultramicrotomed Pt-H-ZSM-22.

sites inside the catalyst (Figure 1 d and Figure S1, Supporting Information). Figure 1 e displays the cross-sections (*ab* plane) of the H-ZSM-22 crystals perpendicular to the *c*-axis. They suggest that a fraction of Pt particles is located inside the H-ZSM-22 crystals, but more Pt particles are deposited on the external surface of the H-ZSM-22 crystals (Figure S2). Pt particles may deposit in and on four possible locations of H-ZSM-22: micropores, mesopores, external surface, and zeolite

crystals (Figure S3). Considering that there are no mesopores in the H-ZSM-22 crystals used and almost no Pt particles smaller than 0.5 nm (Figure 1c), we can exclude the first two options. By counting more than 200 platinum particles from the cross-sections of Pt-H-ZSM-22, around 25% of platinum particles are estimated to be present inside the H-ZSM-22 crystals (Figure S2). The observation that Pt particles inside the zeolite crystals are larger than the micropore channels can be attributed to the collapse of neighboring micropores during the growth of the Pt particles, which was confirmed by Zečević et al. using electron tomography.<sup>[15]</sup> The loading of Pt particles in and on H-ZSM-22 crystals has no significant impact on zeolite porosity (Table S1). Although Pt-H-ZSM-22 shows a heterogeneous distribution of Pt particles, this catalyst still provides the closest proximity between Pt and acid sites.

Pt-H-ZSM-22 was subsequently mixed with boehmite to form a composite bifunctional catalyst with an equal mixture of zeolite and  $\gamma$ -alumina binder (50 wt% each). The HAADF-STEM image of the ultramicrotomed sections of Pt-H-ZSM-22/ $\text{Al}_2\text{O}_3$  confirms that Pt particles with an average size of 1.6 nm are still exclusively located on or inside the zeolite crystals (Figure 2a), while Pt- $\text{Al}_2\text{O}_3$ /H-ZSM-22 shows the Pt particles (1.9 nm) exclusively located on the alumina binder, which provides a nanoscale distance between Pt and acid sites (Figure 2b). The alumina binder has a mesoporous structure with a pore diameter of  $\approx 14$  nm (Table S1 and Figure S4), which is readily accessible for linear and branched  $\text{C}_7$  hydrocarbon molecules. The inductively

coupled plasma (ICP) analysis shows that the Pt loading of Pt-H-ZSM-22/ $\text{Al}_2\text{O}_3$  and Pt- $\text{Al}_2\text{O}_3$ /H-ZSM-22 are 0.6 wt% and 0.5 wt%, respectively (Table S2). For the acid function, the  $\text{NH}_3$ -TPD suggests that these two catalysts have similar acid densities (Figure S5). The ratios of accessible platinum atoms relative to acid sites ( $n_{\text{Pt}}/n_{\text{A}}$ ) for Pt-H-ZSM-22/ $\text{Al}_2\text{O}_3$  and Pt- $\text{Al}_2\text{O}_3$ /H-ZSM-22 are 0.17 and 0.12, respectively (Table S2), sufficient to maintain the metal-acid balance needed for so-called ideal hydrocracking.<sup>[6,7]</sup> In this work, we confirm that even a loading of 0.05 wt% Pt is sufficient for catalysis (Figure S6), that is, the dehydrogenation and hydrogenation reactions can reach quasi-equilibrium.<sup>[16]</sup> Overall, the most significant difference between these two catalysts is the Pt location. Therefore, we can evaluate the impact of nanoscale proximity on the hydroisomerization of *n*-heptane.

Pt- $\text{Al}_2\text{O}_3$ /H-ZSM-22 offers a slightly higher activity than Pt-H-ZSM-22/ $\text{Al}_2\text{O}_3$  in the hydroconversion of *n*-heptane (Figure 2c). The Arrhenius plots (*n*-heptane conversion < 20%) show that for Pt- $\text{Al}_2\text{O}_3$ /H-ZSM-22, the activation energy of the isomerization reaction is 164  $\text{kJ mol}^{-1}$ , which is higher than the value of 147  $\text{kJ mol}^{-1}$  for Pt-H-ZSM-22/ $\text{Al}_2\text{O}_3$  (Figure S7). It is acknowledged that the isomerization reaction on acid sites is the rate-determining step for the hydroisomerization of linear alkanes.<sup>[17]</sup> The difference in activation energies over Pt-H-ZSM-22/ $\text{Al}_2\text{O}_3$  and Pt- $\text{Al}_2\text{O}_3$ /H-ZSM-22 is probably due to the diffusion effects inferred by the location of the platinum. The yield of  $\text{C}_7$  isomers is the most important performance indicator. For Pt- $\text{Al}_2\text{O}_3$ /H-ZSM-22, the nanoscale distance between Pt and acid sites offers

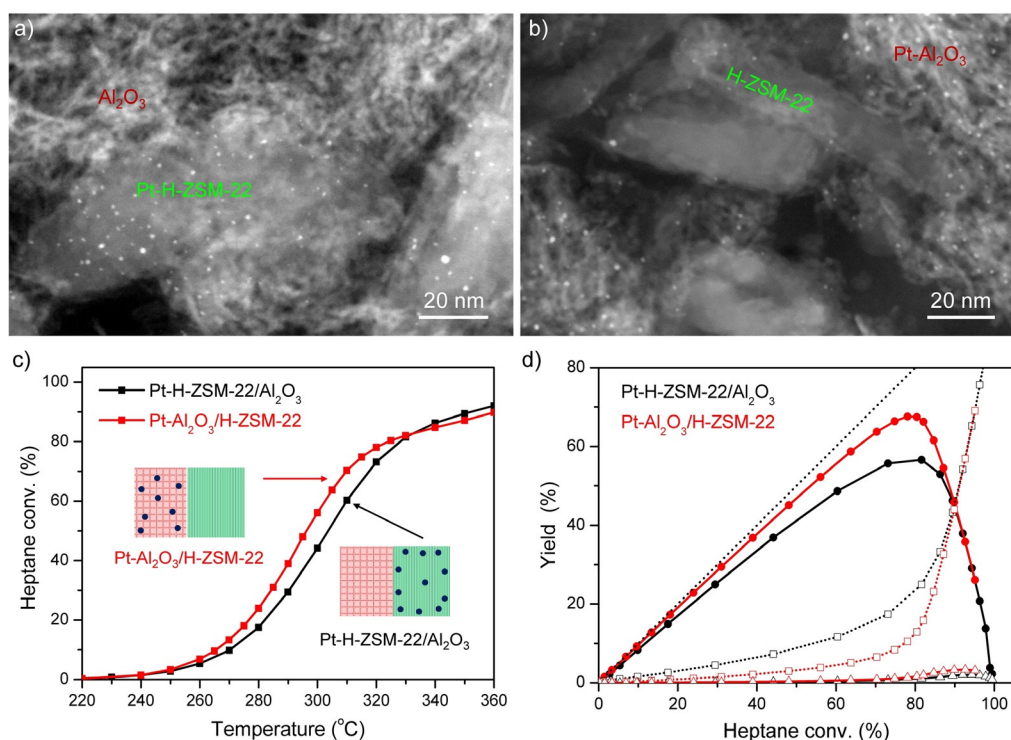


**Figure 2.** HAADF-STEM images with ultramicrotomy of a) Pt-H-ZSM-22/ $\text{Al}_2\text{O}_3$  with Pt in and on the zeolite crystals and b) Pt- $\text{Al}_2\text{O}_3$ /H-ZSM-22 with Pt on the alumina binder. Impact of the Pt location on activities and yields of *n*-heptane hydroconversion over Pt-H-ZSM-22/ $\text{Al}_2\text{O}_3$  (black) and Pt- $\text{Al}_2\text{O}_3$ /H-ZSM-22 (red): c) *n*-heptane conversion vs. reaction temperature; d) yields of total  $\text{C}_7$  isomers (solid lines with solid circles), dibranched  $\text{C}_7$  isomers (solid lines with open triangles), and cracking products (dashed lines with open squares).

a higher yield of  $C_7$  isomers and a lower yield of cracking products than for Pt-H-ZSM-22/ $Al_2O_3$ , where the closest proximity is present (Figure 2d). The main byproducts are  $C_3$  and  $C_4$  alkanes from acid cracking. For both catalysts, the main  $C_7$  isomers are monobranched and the yield of dibranched isomers is lower than 2% ( $n$ -heptane conversion < 80%). From a thermodynamic point of view, the equilibrium composition of dibranched  $C_7$  isomers is comparable to that of monobranched isomers within our reaction-temperature range (Figure S8). The formation of dibranched  $C_7$  isomers needs consecutive isomerization of monobranched  $C_7$  isomers (Figure S9a).<sup>[18]</sup> One should note that due to the narrow channel structure of H-ZSM-22, the isomerization of  $n$ -alkanes over H-ZSM-22 mainly takes place in the pore-mouth region, which is described as pore-mouth catalysis.<sup>[19]</sup> Therefore, the formation of dibranched  $C_7$  isomers is strongly impeded over the H-ZSM-22 catalyst.<sup>[20]</sup> Overall, keeping the proximity between Pt and acid sites in H-ZSM-22 at a nanoscale distance is beneficial for both activity and product selectivity.

Figure 3 shows the product selectivities over Pt-H-ZSM-22/ $Al_2O_3$  and Pt- $Al_2O_3$ /H-ZSM-22 at the temperature where their yield of  $C_7$  isomers reaches the maximum. The side reactions of  $n$ -heptane hydroisomerization may include acid cracking, hydrogenolysis, and dimerization cracking.<sup>[6c,21]</sup> The main cracking products for both catalysts are propane, butane, and *iso*-butane. One feature of the H-ZSM-22-based catalyst is that it favors the formation of  $n$ -alkanes such as  $n$ -butane,  $n$ -pentane, and  $n$ -hexane in cracking reactions. For example, the fraction of  $n$ -butane in  $C_4$  products is higher than 50% over Pt-H-ZSM-22/ $Al_2O_3$ , while the value over H-ZSM-5 and H-beta-based catalysts is lower than 10%.<sup>[22]</sup> Furthermore, the Pt-H-ZSM-22/ $Al_2O_3$  catalyst produced many more cracking products than the Pt- $Al_2O_3$ /H-ZSM-22 catalyst (Figure 3). It is also noteworthy that the Pt-H-ZSM-22/ $Al_2O_3$  catalyst with the closest proximity between metal and acid sites also produced more methane and ethane than the

Pt- $Al_2O_3$ /H-ZSM-22 catalyst with nanoscale proximity. The formation of methane and ethane could be indicative of hydrogenolysis or the formation of primary carbenium ions.<sup>[5]</sup> Choudhury et al. attributed the formation of methane and ethane to an (s,p)- $\beta$ -scission reaction, which was described as the acid cracking of secondary alkylcarbenium ions into primary ones inside the H-ZSM-22 micropore channels (Figure S9b).<sup>[23]</sup> It is only under the severe confinement inside narrow micropores with a high density of acid sites that the energetically unfavorable (s,p)- $\beta$ -scission contributes significantly to the overall product distribution. The formation of smaller  $n$ -alkanes is a confirmation that cracking reactions over H-ZSM-22 catalysts take place inside the narrow micropore channels to a large extent,<sup>[23]</sup> otherwise the cracking products with  $\geq 4$  carbon atoms should be mostly branched. Therefore, placing Pt sites (even a fraction of them) inside the H-ZSM-22 crystals imposes more undesired cracking reactions than on the binder.

### H-MOR-Based Catalysts with 12-MR Micropores with Different Micropore Lengths

The mordenite structure contains straight 12-MR channels of  $0.65 \times 0.70$  nm size interconnected by 8-MR pores of  $0.34 \times 0.48$  nm size. Because the 8-MR channels are inaccessible to molecules larger than methane, the mordenite structure is generally considered to be one-dimensional.<sup>[24]</sup> H-MOR-S with small crystals has an average crystallite size of  $\approx 200$  nm, as evidenced from measuring the long sides of scattered crystals (Figure 4a). The 1D micropore channels of mordenite are also oriented along the  $c$ -axis, as in H-ZSM-22, but the quantification of the micropore length for H-MOR-S is difficult due to the irregular morphology (Figure 4a). H-MOR-L with a plate-like morphology was synthesized by a seed-induced method using H-MOR-S as a starting material, which can also be regarded as an epitaxial-growth process on the parent H-MOR-S planes. Thus, the diffusion length of H-MOR-L (Figure 4b) should be longer than in the parent compound H-MOR-S. The fast Fourier transform (FFT) of the HRTEM image suggests that the surface of the plate-like crystals is essentially the  $ab$ -plane, which is perpendicular to the 12-MR channels (Figure S10). The average micropore length for H-MOR-L is  $\approx 300$  nm, which is significantly larger than the average crystallite size of H-MOR-S ( $\approx 200$  nm). In fact, the actual difference in the diffusion length of H-MOR-S and H-MOR-L should be much more than 100 nm due to the irregular morphology of H-MOR-S. These two mordenites have very similar crystallinities and Si/Al ratios (Figure S11 and Table S1), so the crucial difference is the average diffusion length through the micropore channels.

In contrast to Pt-H-ZSM-22/ $Al_2O_3$ , which shows a non-uniform distribution of platinum particles, the HAADF-STEM image of the catalyst sections confirms that Pt particles with diameters of 1.5–1.6 nm are well-distributed across the zeolite crystals for Pt-H-MOR-S/ $Al_2O_3$  and Pt-H-MOR-L/ $Al_2O_3$  (Figure 4c,d and Table S2). One could expect that  $Pt(NH_3)_4^{2+}$  ions (0.48 nm) can easily diffuse into mordenite micropores ( $0.65 \times 0.70$  nm) in the ion-exchange step. The fact

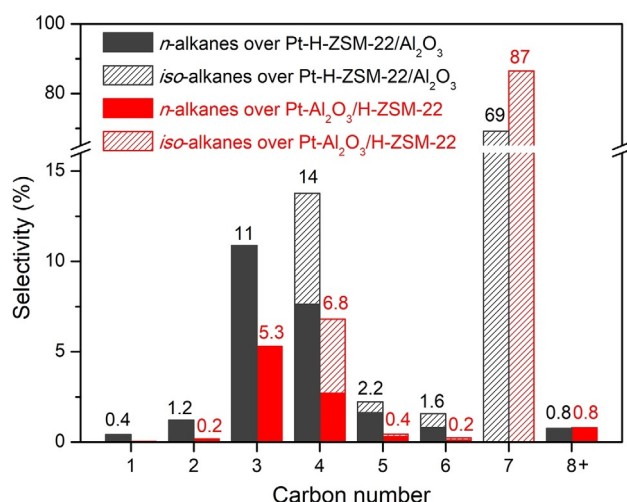


**Figure 3.** Product selectivity over Pt-H-ZSM-22/ $Al_2O_3$  (black) at 330 °C with an  $n$ -heptane conversion of 81.6%, and over Pt- $Al_2O_3$ /H-ZSM-22 (red) at 320 °C with an  $n$ -heptane conversion of 78.1%.  $C_{8+}$  denotes hydrocarbon products with 8 or more carbon atoms.

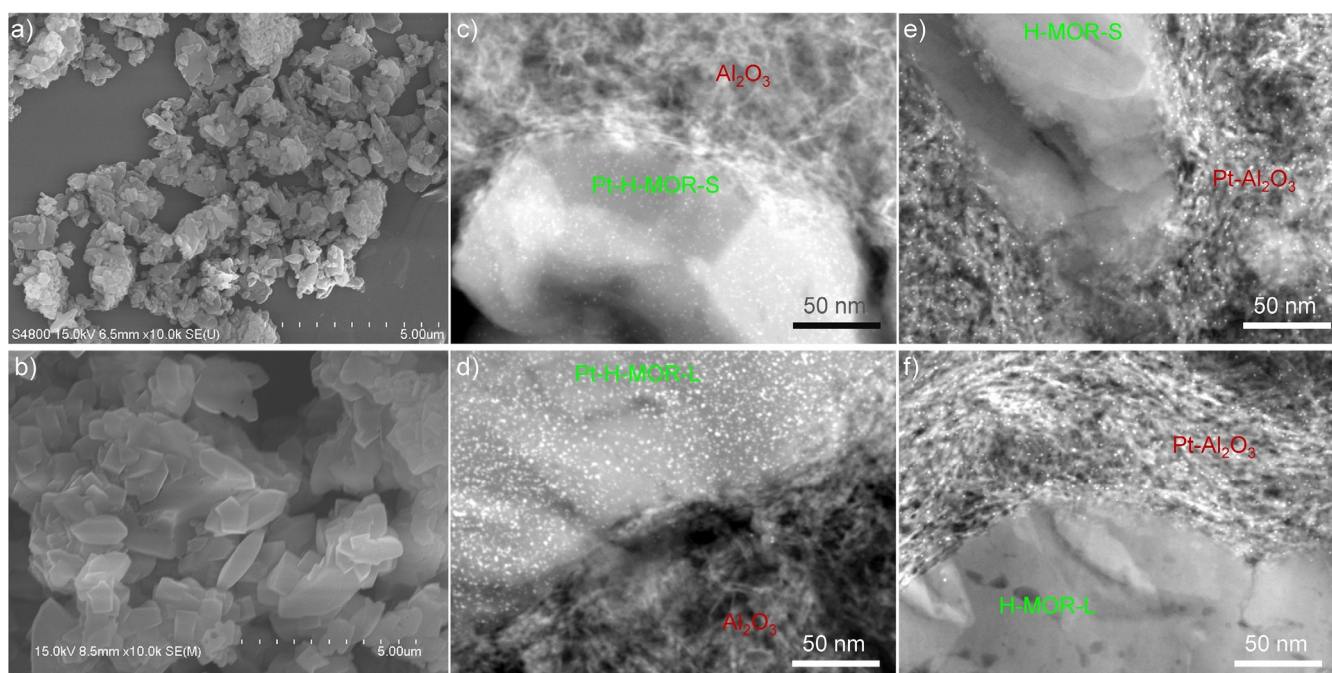


**Figure 4.** SEM images of a) H-MOR-S and b) H-MOR-L. HAADF-STEM images with ultramicrotomy of c) Pt-H-MOR-S/ $\text{Al}_2\text{O}_3$  and d) Pt-H-MOR-L/ $\text{Al}_2\text{O}_3$  (closest proximity), e) Pt- $\text{Al}_2\text{O}_3$ /H-MOR-S, and f) Pt- $\text{Al}_2\text{O}_3$ /H-MOR-L (nanoscale proximity).

that the Pt particle size is larger than the MOR micropores points to a local collapse of micropores upon particle growth<sup>[15]</sup> when platinum particles are still surrounded by micropores, as shown in position 4 of Figure S3. Additionally, platinum particles were also exclusively deposited on the alumina binder for Pt- $\text{Al}_2\text{O}_3$ /H-MOR-S and Pt- $\text{Al}_2\text{O}_3$ /H-MOR-L (Figure 4e,f). The average Pt particle sizes of these four samples are in the range of 1.5–1.8 nm, while the Pt loadings are in the range of 0.5–0.6 wt % (Table S2).  $\text{NH}_3$ -TPD confirms very similar acidities for the four catalysts (Figure S12). Therefore, these four catalysts with identical metal function and acid density allow us to evaluate the impact of nanoscale intimacy between metal and acid sites, and the effect of crystal size on *n*-heptane hydroisomerization.

The Pt-H-MOR-S/ $\text{Al}_2\text{O}_3$  with closest intimacy between Pt and acid sites provided a similar activity as Pt- $\text{Al}_2\text{O}_3$ /H-MOR-S with a nanoscale distance between the sites (Figure 5a). Regarding the yield of desired  $\text{C}_7$  isomers, similar to H-ZSM-22-based catalysts, the Pt- $\text{Al}_2\text{O}_3$ /H-MOR-S exhibited a higher yield of  $\text{C}_7$  isomers and lower yield of cracking products than Pt-H-MOR-S/ $\text{Al}_2\text{O}_3$  (Figure 5c). The yield of dibranched isomers over H-MOR-S-based catalysts is much higher than over H-ZSM-22-based catalysts (Figure 2d and 5c), because the consecutive skeletal isomerization can take place inside the 12-MR micropore channels.<sup>[25]</sup> Specifically, the maximum yield of dibranched isomers over Pt- $\text{Al}_2\text{O}_3$ /H-MOR-S was 9.4% at a *n*-heptane conversion level of  $\approx 80\%$ , while the corresponding value over Pt- $\text{Al}_2\text{O}_3$ /H-ZSM-22 is 1.3%. However, the dibranched isomers are susceptible to cracking into  $\text{C}_3$  and  $\text{C}_4$  hydrocarbons (Figure S9b). The maximum yield of  $\text{C}_7$  isomers over Pt- $\text{Al}_2\text{O}_3$ /H-MOR-S is 57%, which is significantly lower than the value of 68% over Pt- $\text{Al}_2\text{O}_3$ /H-

ZSM-22. Placing Pt particles inside the H-MOR-S crystals (Pt-H-MOR-S/ $\text{Al}_2\text{O}_3$ ) further decreases the yield to 51%. Therefore, placing Pt particles inside H-MOR-S crystals is also detrimental for the yield of  $\text{C}_7$  isomers.

Compared with the two H-MOR-S-based catalysts, the activities of the two H-MOR-L-based catalysts are lower (Figure 5a,b). Considering that the density of Pt and acid sites are similar for these four catalysts (Table S2 and Figure S12), the difference in activity between H-MOR-S and H-MOR-L should be caused by the accessibility of active sites: the acid sites deep inside the H-MOR-L crystals do not significantly participate in the isomerization reaction.<sup>[26]</sup> It was revealed that the adsorption of linear alkanes in the zeolite is dominated by van-der-Waals interactions, but linear alkenes are additionally stabilized by the formation of a  $\pi$ -complex or alkoxide with BAS with stronger adsorption energies.<sup>[27]</sup> Here, the oxygen atoms (Si-O-Al) on the zeolite framework can act as nucleophilic centers, interacting with the carbon atoms of alkenes to form alkoxides. This phenomenon was experimentally confirmed by propene-TPD and propane-TPD (Figure S13), which confirmed the enrichment of immobile olefinic species in acid zeolites. The activation energies for the H-MOR-L-based catalysts were systematically lower than for the H-MOR-S-based catalysts (Figure S7), which suggests mass-transfer limitations over zeolites with large crystals.<sup>[9,28]</sup> The apparent turnover frequency (TOF) based on BAS was also lower over H-MOR-L-based catalysts than H-MOR-S-based catalysts (Figure S14), indicating that the effective utilization of acid sites is influenced by the diffusion length of the zeolite crystals. The lower activity of Pt- $\text{Al}_2\text{O}_3$ /H-MOR-L in comparison to Pt-H-MOR-L/ $\text{Al}_2\text{O}_3$  is not understood well, but it is probably due to the long diffusion-path length between active platinum and acid sites for Pt- $\text{Al}_2\text{O}_3$ /H-MOR-

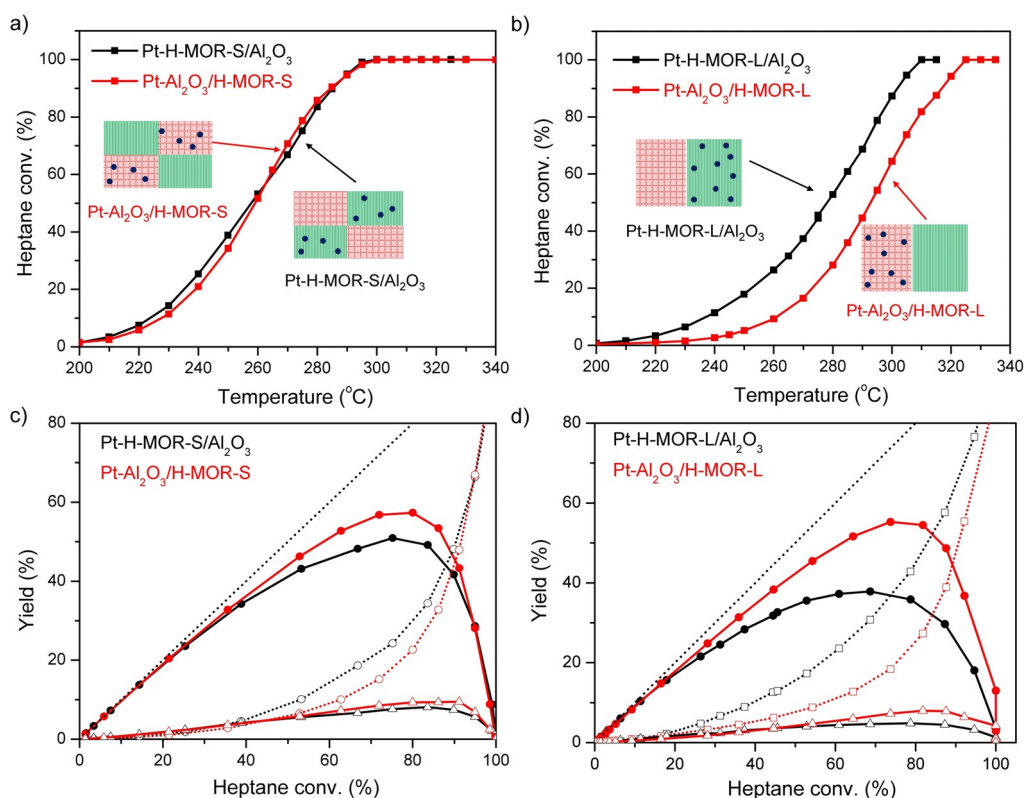


**Figure 5.** Impact of the platinum location on *n*-heptane conversion over Pt-H-MOR-S/Al<sub>2</sub>O<sub>3</sub>, Pt-Al<sub>2</sub>O<sub>3</sub>/H-MOR-S, Pt-H-MOR-L/Al<sub>2</sub>O<sub>3</sub>, and Pt-Al<sub>2</sub>O<sub>3</sub>/H-MOR-L. a), b) *n*-heptane conversion vs. reaction temperature. c), d) Yields of total C<sub>7</sub> isomers (solid lines with solid circles), dibranched C<sub>7</sub> isomers (solid lines with open triangles), and cracked products (dashed lines with open squares).

L, in line with the criterion by Weisz. It should be noted that at low reaction rates, that is, at low conversion levels, placing platinum inside H-MOR-L crystals was found to be beneficial for the TOF<sub>BAS</sub> value (Figure S14).

The mordenite-based catalysts produced almost no methane and ethane (<0.2%) even at 320 °C, and most C<sub>4</sub>–C<sub>6</sub> products were *iso*-alkanes from acid cracking (Figure 6). This distribution suggests that β-scission reactions with tertiary-to-secondary and secondary-to-tertiary modes are favored over mordenite catalysts (Figure S9b). Additionally, the formation of C<sub>5</sub>, C<sub>6</sub>, and C<sub>8+</sub> products (without formation of methane and ethane) indicates that dimerization cracking also contributes to a low extent. Regarding the impact of proximity, the Pt-H-MOR-L/Al<sub>2</sub>O<sub>3</sub> catalyst with Pt sites inside the zeolite crystals displays a maximum yield of C<sub>7</sub> isomers as low as 38% (Figure 5d). In the case of the bifunctional catalyst with Pt sites inside H-MOR-L crystals, conversion of *n*-heptane has to take place inside the narrow micropores due to the fact that the majority of Pt and acid sites are inside the mordenite crystals. The long diffusion channels cause strong diffusion limitations, especially for branched alkene intermediates, leading to severe acid-cracking reactions. The selectivity of cracking products in the C<sub>3</sub>–C<sub>6</sub> range over the Pt-H-MOR-L/Al<sub>2</sub>O<sub>3</sub> catalyst was two times as high as that over Pt-Al<sub>2</sub>O<sub>3</sub>/H-MOR-L. Interestingly, the maximum yield of C<sub>7</sub> isomers over Pt-Al<sub>2</sub>O<sub>3</sub>/H-MOR-L was 55%, which is close to 57% over Pt-Al<sub>2</sub>O<sub>3</sub>/H-MOR-S, which features a short diffusion length. Aside from this, the product selectivity was

almost the same for these two Pt-on-binder catalysts (Figure S15). Based on these findings, we believe that in the case of Pt-on-binder catalysts, most isomerization reactions take

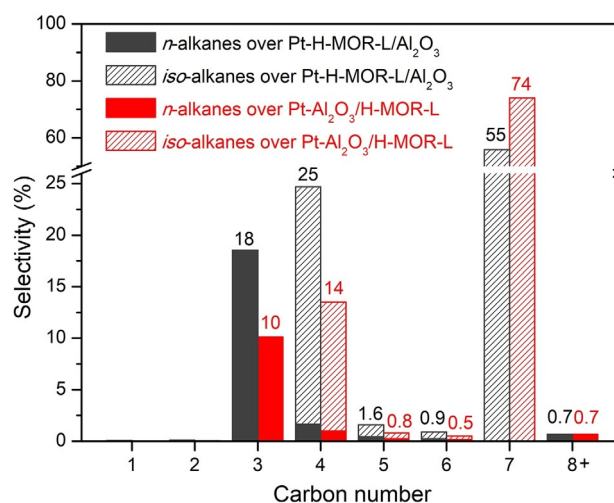


**Figure 6.** The impact of the platinum location on the product distribution. Product selectivity over Pt-H-MOR-L/Al<sub>2</sub>O<sub>3</sub> (black) at 290 °C with an *n*-heptane conversion of 69%, and Pt-Al<sub>2</sub>O<sub>3</sub>/H-MOR-L (red) at 305 °C with an *n*-heptane conversion of 74%. C<sub>8+</sub> denotes hydrocarbon products with 8 or more carbon atoms. Catalytic behaviors at identical temperatures are listed in Table S3.

place in the pore-mouth region of the zeolite, even for mordenite with long 12-MR micropore channels.

### Reaction Mechanisms

We have investigated the nanoscale intimacy in 1D zeolite-based bifunctional catalysts for *n*-heptane hydroisomerization. Our findings demonstrate that the intimacy between Pt and acid sites, especially at the nanoscale, has a significant influence on catalytic activity and selectivity. Specifically, when using H-ZSM-22 with 10-MR channels, the controlled deposition of Pt particles exclusively on the alumina binder is beneficial for both catalytic activity and yield of  $C_7$  isomers. Most  $C_7$  isomers are monobranched due to the mechanism of pore-mouth catalysis. The diffusion of both *n*-heptane and *iso*-alkenes to platinum sites is fast when platinum is located on the alumina binder (Figure 7a). Once the *n*-heptenes are isomerized in the pore mouths of the zeolite, it is faster for *iso*-heptenes to diffuse out of the channels and back to platinum sites for hydrogenation than to diffuse into the H-ZSM-22 channels for further isomerization and cracking. For the Pt-H-ZSM-22/ $Al_2O_3$  catalyst, the spatial distribution of platinum over Pt-H-ZSM-22 is non-uniform with around 25 % of platinum particles inside the crystals. The Pt particles on the external surface of the H-ZSM-22 crystals can still catalyze the (de)hydrogenation, acting the same as Pt particles on the alumina binder. We propose that platinum particles inside the H-ZSM-22 crystals lower the yield of  $C_7$  isomers because *n*-heptane feedstock can diffuse relatively rapidly inside its channels and get converted, giving rise to secondary cracking reactions due to diffusion constraints (Figure 7a). The formation of linear butane and pentane over the H-ZSM-22 catalysts, especially with platinum particles

inside the zeolite crystals, strongly suggests that a significant fraction of cracking reactions takes place inside the zeolite channels.

In the case of mordenite-based bifunctional catalysts, the yield of dibranched isomers for mordenite-based catalysts is generally higher than that for H-ZSM-22-based catalysts. The activity is not affected by whether the Pt particles reside on the alumina binder or inside the 12-MR channels when using small mordenite crystals. Different to Pt-H-ZSM-22, the vast majority of platinum particles for Pt-H-MOR-S is located inside zeolite crystals, because the micropore size of mordenite is larger than  $Pt(NH_3)_4^{2+}$  ions. The *n*-heptane feedstock and alkene intermediates can diffuse quickly to active sites for (de)hydrogenation and isomerization (Figure 7b). However, locating Pt particles inside the zeolite crystals with closest intimacy produces more acid-cracking products than for Pt-on-binder catalysts. This detrimental influence is intensified when using mordenite, which has a long diffusion length. The similarity in product selectivity for the two Pt-on-binder catalysts with distinct crystal sizes suggests that the isomerization reaction over mordenite also follows the general pore-mouth-catalysis mechanism.

Our previous study based on Y zeolite (crystal size 0.5–1.0  $\mu m$ ) with a 3D micropore network and 12-MR channels showed that placing platinum particles inside zeolite crystals favors the cracking reaction compared with placing platinum on the alumina binder in the hydroconversion of  $C_{10}$ – $C_{19}$  paraffins.<sup>[10]</sup> Recently, Moussa et al. also reported a nanosized beta-zeolite system, where placing platinum on the alumina binder outperformed embedding platinum particles inside the crystals of the beta-zeolite in *n*-heptane isomerization at atmospheric pressure.<sup>[11b]</sup> Therefore, the influence of nanoscale intimacy still exists when using 3D crystals, albeit in interplay with the molecular size of the reactant.

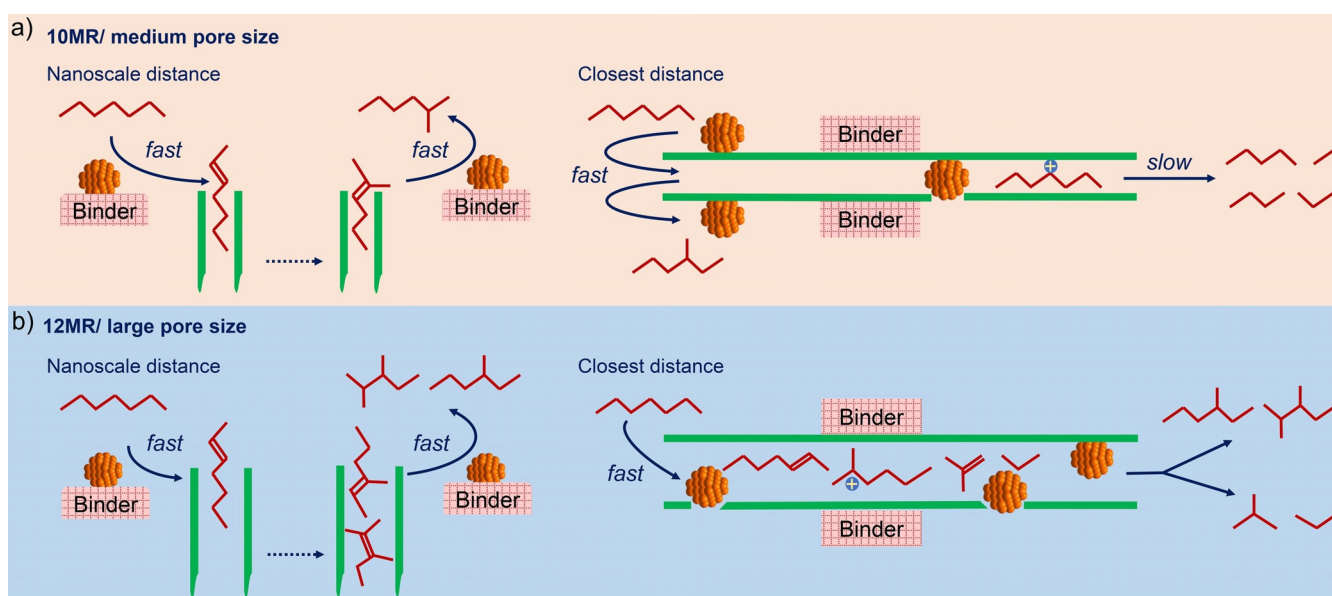


**Figure 7.** Schematic representation of the impact of spatial organization of platinum inside or outside the zeolites on *n*-heptane hydroisomerization. a) H-ZSM-22-based catalysts with different proximity between Pt and acid sites. b) Mordenite-based catalysts with different proximity between Pt and acid sites.

To further investigate the scope of nanoscale proximity on *n*-heptane hydroisomerization, we evaluated the effect of platinum location over H-ZSM-5-based catalysts with a 3D micropore network. H-ZSM-5 consisting of aggregates of  $\approx 40$  nm crystals was used to construct bifunctional catalysts to minimize the diffusion limitations (Figure S16). We have controlled the platinum location either inside the H-ZSM-5 crystals or on the alumina binder (Figure S17). The catalytic performances show that the location of the platinum particles does not affect the activity and the *iso*-C<sub>7</sub> yield for *n*-heptane hydroisomerization (Figure S18). However, it should be noted that the *iso*-butane-to-*n*-butane ratio over Pt-H-ZSM-5/Al<sub>2</sub>O<sub>3</sub> is significantly lower than over Pt-Al<sub>2</sub>O<sub>3</sub>/H-ZSM-5 (Figure S18c), indicating that the energetically unfavorable secondary-to-secondary cracking reactions (Figure S9b) tend to take place more extensively inside the H-ZSM-5 micropores. Therefore, the platinum location still has an influence on product selectivities for H-ZSM-5 with a 3D pore structure. Vandegehuchte et al. reported that in *n*-hexane hydroconversion, branched isomers would suffer from strong intracrystalline diffusion limitations in H-ZSM-5 crystallites, but the limitations could be mitigated by decreasing the size of the H-ZSM-5 crystals.<sup>[29]</sup> In fact, decreasing the effective crystal sizes of zeolites and building hierarchical structures has often been employed to increase the isomer selectivity over H-MOR and H-beta catalysts without considering the platinum location.<sup>[30]</sup> We think that the detrimental effect on product selectivity imposed by placing platinum particles inside the zeolite crystals in hydroisomerization reactions is generalizable for zeolites with 1D pore systems and 3D zeolites with long diffusion channels.

## Conclusion

In summary, we succeeded in placing platinum particles either on the alumina binder or inside 1D zeolite crystals, as confirmed by TEM-based characterization using ultramicrotomy. The Pt-on-binder catalyst provides a nanoscale proximity between platinum particles and acid sites, while the catalyst with platinum sites inside the zeolite crystals offers the closest proximity. The catalysis results suggest that embedding the platinum particles imposes undesired cracking reactions inside the narrow micropore channels, so the closest proximity between platinum and acid sites is detrimental for the product selectivity. The extent of the influence of the platinum location is strongly dependent on the dimensionality of the zeolite, the size of the molecules, and the reaction conditions. In the context of numerous efforts being made to place metal particles inside the zeolites, our findings suggest that placing metal particles on the alumina binder may bring many benefits for catalysis. Earlier, this was demonstrated for bulky feedstock molecules while we have now shown this to hold for light reactant molecules, too.

## Acknowledgements

This work has been supported by BP and Topsector Chemie consortia for Knowledge and Innovation (TKIs). K.P.d.J. acknowledges funding from the European Research Council, EU FP7 ERC Advanced Grant no.338846. H.Y. thanks the Program for Advancing Strategic International Networks to Accelerate the Circulation of Talented Researchers by JSPS. Nikolaos Nikolopoulos, Remco Dalebout, Miguel Rivera Torrente and Silvia Zanoni are acknowledged for measuring and analyzing the N<sub>2</sub> physisorption data.

## Conflict of interest

The authors declare no conflict of interest.

**Keywords:** bifunctional catalysis · hydroisomerization · one-dimensional zeolites · spatial proximity · shape selectivity

**How to cite:** *Angew. Chem. Int. Ed.* **2020**, *59*, 3592–3600  
*Angew. Chem.* **2020**, *132*, 3620–3628

- [1] a) B. Peng, Y. Yao, C. Zhao, J. A. Lercher, *Angew. Chem. Int. Ed.* **2012**, *51*, 2072–2075; *Angew. Chem.* **2012**, *124*, 2114–2117; b) D. M. Alonso, J. Q. Bond, J. A. Dumesic, *Green Chem.* **2010**, *12*, 1493–1513; c) F. Jiao, J. Li, X. Pan, J. Xiao, H. Li, H. Ma, M. Wei, Y. Pan, Z. Zhou, M. Li, S. Miao, J. Li, Y. Zhu, D. Xiao, T. He, J. Yang, F. Qi, Q. Fu, X. Bao, *Science* **2016**, *351*, 1065–1068; d) C. Zhou, J. Shi, W. Zhou, K. Cheng, Q. Zhang, J. Kang, Y. Wang, *ACS Catal.* **2020**, *10*, 302–310; e) J. Kim, S. W. Han, J. C. Kim, R. Ryoo, *ACS Catal.* **2018**, *8*, 10545–10554.
- [2] a) K. P. de Jong, *Science* **2016**, *351*, 1030–1031; b) K. Cheng, B. Gu, X. Liu, J. Kang, Q. Zhang, Y. Wang, *Angew. Chem. Int. Ed.* **2016**, *55*, 4725–4728; *Angew. Chem.* **2016**, *128*, 4803–4806; c) J. Li, Y. He, L. Tan, P. Zhang, X. Peng, A. Oruganti, G. Yang, H. Abe, Y. Wang, N. Tsubaki, *Nat. Catal.* **2018**, *1*, 787–793.
- [3] a) J. H. Sinfelt, *Adv. Chem. Eng.* **1964**, *5*, 37–74; b) L. Liu, U. Díaz, R. Arenal, G. Agostini, P. Concepción, A. Corma, *Nat. Mater.* **2017**, *16*, 132–138.
- [4] a) M. Andersen, A. J. Medford, J. K. Nørskov, K. Reuter, *Angew. Chem. Int. Ed.* **2016**, *55*, 5210–5214; *Angew. Chem.* **2016**, *128*, 5296–5300; b) E. L. Margelefsky, A. Bendjériou, R. K. Zeidan, V. Dufaud, M. E. Davis, *J. Am. Chem. Soc.* **2008**, *130*, 13442–13449; c) E. Iglesia, D. G. Barton, J. A. Biscardi, M. J. L. Gines, S. L. Soled, *Catal. Today* **1997**, *38*, 339–360.
- [5] J. Weitkamp, *ChemCatChem* **2012**, *4*, 292–306.
- [6] a) G. Noh, Z. Shi, S. I. Zones, E. Iglesia, *J. Catal.* **2018**, *368*, 389–410; b) M. Guisnet, F. Alvarez, G. Giannetto, G. Perot, *Catal. Today* **1987**, *1*, 415–433; c) N. Batalha, L. Pinard, C. Bouchy, E. Guillon, M. Guisnet, *J. Catal.* **2013**, *307*, 122–131.
- [7] N. Batalha, L. Pinard, Y. Pouilloux, M. Guisnet, *Catal. Lett.* **2013**, *143*, 587–591.
- [8] a) P. B. Weisz, E. W. Swegler, *Science* **1957**, *126*, 31–32; b) P. B. Weisz, *Adv. Catal.* **1962**, *13*, 137–190.
- [9] M. Höchtel, A. Jentys, H. Vinek, *J. Catal.* **2000**, *190*, 419–432.
- [10] J. Zecevic, G. Vanbutsele, K. P. de Jong, J. A. Martens, *Nature* **2015**, *528*, 245–248.
- [11] a) J. E. Samad, J. Blanchard, C. Sayag, C. Louis, J. R. Regalbutto, *J. Catal.* **2016**, *342*, 203–212; b) O. Ben Moussa, L. Tinat, X. Jin, W. Baaziz, O. Durupthy, C. Sayag, J. Blanchard, *ACS Catal.* **2018**, *8*, 6071–6078.



- [12] a) A. Chica, A. Corma, P. J. Miguel, *Catal. Today* **2001**, *65*, 101–110; b) D. Verboekend, K. Thomas, M. Milina, S. Mitchell, J. Perez-Ramirez, J. P. Gilson, *Catal. Sci. Technol.* **2011**, *1*, 1331–1335; c) J. A. Martens, D. Verboekend, K. Thomas, G. Vanbutsele, J. P. Gilson, J. Pérez-Ramírez, *ChemSusChem* **2013**, *6*, 421–425; d) S. Liu, J. Ren, H. Zhang, E. Lv, Y. Yang, Y. W. Li, *J. Catal.* **2016**, *335*, 11–23; e) N. Li, F. Jiao, X. Pan, Y. Chen, J. Feng, G. Li, X. Bao, *Angew. Chem. Int. Ed.* **2019**, *58*, 7400–7404; *Angew. Chem.* **2019**, *131*, 7478–7482.
- [13] B. Smit, T. L. M. Maesen, *Chem. Rev.* **2008**, *108*, 4125–4184.
- [14] M. Schreier, S. Teren, L. Belcher, J. R. Regalbuto, J. T. Miller, *Nanotechnology* **2005**, *16*, S582–S591.
- [15] J. Zečević, A. M. J. van der Eerden, H. Friedrich, P. E. de Jongh, K. P. de Jong, *ACS Nano* **2013**, *7*, 3698–3705.
- [16] E. G. Acebo, C. Leroux, C. Chizallet, Y. Schuurman, C. Bouchy, *ACS Catal.* **2018**, *8*, 6035–6046.
- [17] a) Y. Ono, *Catal. Today* **2003**, *81*, 3–16; b) A. Holló, J. Hancsók, D. Kalló, *Appl. Catal. A* **2002**, *229*, 93–102; c) G. F. Froment, *Catal. Today* **1987**, *1*, 455–473.
- [18] V. M. Akhmedov, S. H. Al-Khowaiter, *Catal. Rev.* **2007**, *49*, 33–139.
- [19] a) J. A. Martens, W. Souverijns, W. Verrelst, R. Parton, G. F. Froment, P. A. Jacobs, *Angew. Chem. Int. Ed. Engl.* **1995**, *34*, 2528–2530; *Angew. Chem.* **1995**, *107*, 2726–2728; b) W. Souverijns, J. A. Martens, G. F. Froment, P. A. Jacobs, *J. Catal.* **1998**, *174*, 177–184; c) C. S. Laxmi Narasimhan, J. W. Thybaut, G. B. Marin, J. A. Martens, J. F. Denayer, G. V. Baron, *J. Catal.* **2003**, *218*, 135–147.
- [20] J. A. Martens, G. Vanbutsele, P. A. Jacobs, J. Denayer, R. Ocakoglu, G. Baron, J. A. Muñoz Arroyo, J. Thybaut, G. B. Marin, *Catal. Today* **2001**, *65*, 111–116.
- [21] F. J. M. M. de Gauw, J. van Grondelle, R. A. van Santen, *J. Catal.* **2001**, *204*, 53–63.
- [22] a) Z. B. Wang, A. Kamo, T. Yoneda, T. Komatsu, T. Yashima, *Appl. Catal. A* **1997**, *159*, 119–132; b) J. Kim, W. Kim, Y. Seo, J. C. Kim, R. Ryoo, *J. Catal.* **2013**, *301*, 187–197.
- [23] I. R. Choudhury, K. Hayasaka, J. W. Thybaut, C. S. Laxmi Narasimhan, J. F. Denayer, J. A. Martens, G. B. Marin, *J. Catal.* **2012**, *290*, 165–176.
- [24] C. E. Webster, A. Cottone, R. S. Drago, *J. Am. Chem. Soc.* **1999**, *121*, 12127–12139.
- [25] F. Jiménez-Cruz, G. C. Laredo, *Fuel* **2004**, *83*, 2183–2188.
- [26] C. Pagis, F. Meunier, Y. Schuurman, A. Tuel, M. Dodin, R. Martinez-Franco, D. Farrusseng, *ChemCatChem* **2018**, *10*, 4525–4529.
- [27] a) B. A. De Moor, M. F. Reyniers, G. B. Marin, *Phys. Chem. Chem. Phys.* **2009**, *11*, 2939–2958; b) R. J. Correa, C. J. A. Mota, *Phys. Chem. Chem. Phys.* **2002**, *4*, 375–380.
- [28] G. Ye, Y. Sun, Z. Guo, K. Zhu, H. Liu, X. Zhou, M. O. Coppens, *J. Catal.* **2018**, *360*, 152–159.
- [29] a) B. D. Vandegheuchte, J. W. Thybaut, G. B. Marin, *Ind. Eng. Chem. Res.* **2014**, *53*, 15333–15347; b) B. D. Vandegheuchte, I. R. Choudhury, J. W. Thybaut, J. A. Martens, G. B. Marin, *J. Phys. Chem. C* **2014**, *118*, 22053–22068.
- [30] a) J. Pastvova, D. Kaucky, J. Moravkova, J. Rathousky, S. Sklenak, M. Vorokhta, L. Brabec, R. Pilar, I. Jakubec, E. Tabor, P. Klein, P. Sazama, *ACS Catal.* **2017**, *7*, 5781–5795; b) F. Bauer, K. Ficht, M. Bertmer, W. D. Einicke, T. Kuchling, R. Gläser, *Catal. Sci. Technol.* **2014**, *4*, 4045–4054; c) M. Tromp, J. A. van Bokhoven, M. T. Garriga Oostenbrink, J. H. Bitter, K. P. de Jong, D. C. Koningsberger, *J. Catal.* **2000**, *190*, 209–214.

Manuscript received: November 26, 2019

Accepted manuscript online: December 21, 2019

Version of record online: January 22, 2020